Some Solved and Unsolved Problems in Transmission Electron Microscopy Studies of Radiation Damage in Solids*

S.E. Donnelly**

Institute for Materials Research, University of Salford
Greater Manchester M5 4WT, UK

Abstract

Solved and unsolved questions from fifteen years of research using transmission electron microscopy in the study of radiation damage in materials are discussed. Examples are presented on topics that include single-ion impacts on metal surfaces, helium bubbles in semiconductors, solid xenon precipitates in metals and single-ion induced amorphous zones in silicon.

Contents

* This paper makes extensive reference to video recordings of *in-situ* TEM experiments for which video-clips are available at: http://www.imr.salford.ac.uk/fm/sed/media.php

** E-mail: s.e.donnelly@salford.ac.uk

1. Introduction

Transmission electron microscopy (TEM) has been used in the study of radiation damage in solids almost since the beginning of such studies; however, in recent decades, the ever-improving resolution of microscopes has enabled researchers to resolve defect structures resulting from single ion impacts, rendering this a very powerful experimental tool. In addition, in a small number of laboratories around the world, facilities exist in which it is possible to ion-irradiate thin foils *in-situ* in a TEM. These facilities add an important dimension by allowing observation of ion-induced defect morphologies as they develop during continuous ion irradiation.

The author has spent 15 years using an *in-situ* TEM/ion irradiation facility at Argonne National Laboratory, USA and has also collaborated on experiments using a high voltage electron microscope at the National Institute for Materials Science in Tsukuba, Japan. In this latter machine, displacement damage is created by the electrons used for imaging. In both these facilities, experiments have been conducted that have yielded unique insights into radiation damage processes.

This paper is an attempt to elucidate the problems in ion beam physics that have been solved by this approach and also to discuss those problems that remain to be solved. Work will be presented on single-ion impacts on metal surfaces, inert gas bubbles in semiconductors and metals and single-ion induced amorphous zones in silicon.

2. Thermal Spike-Induced Plastic Flow

2.1. Background

Above a certain energy density, the interaction of an energetic ion with a solid can no longer be successfully described as an orderly series of binary collisions involving the impinging ion and recoiling substrate atoms. As first suggested by Brinkman (1954), when the mean free path between displacing collisions approaches the interatomic spacing of the substrate, this description breaks down and instead one must think in terms of the formation of a small highly disturbed region, in which the mean kinetic energy of the atoms may be up to several eV, known as an energy or displacement spike. At some time after the initial energy deposition (of order tens of picoseconds), the kinetic energy in the spike may be shared in a continuous distribution by all the atoms within the spike region. Under some conditions this may give rise to an effective temperature within the spike zone significantly above that required for melting – this phase is generally referred to as a thermal spike.

Spikes resulting from single ion impacts were first discussed in the scientific literature more than 50 years ago; experimentally, however, until much more recently it has been difficult to study the effects of individual spikes as they are both small – typically of the order of a few nanometres in diameter – and of short duration – of order tens of picoseconds. Obtaining information on spikes resulting from individual ions thus necessitates techniques with a high spatial resolution. Unfortunately, no technique with adequate spatial resolution has a temporal resolution within orders of magnitude of spike lifetimes so that, as far as temporal resolution is concerned, observations are always of morphologies that include the effects of the displacement spike, the thermal spike and any ensuing defect annealing processes that may take place on timescales of milliseconds or more.

Over the last 30 years or so, as mentioned in the Introduction, the resolution of electron microscopes has improved and advances in the speed and capacity of computers have enabled the accurate modeling of larger and larger assemblies of atoms using molecular dynamics (MD) simulations. With this convergence, it is now possible both to image individual spike effects in the transmission electron microscope and to perform MD simulations of spike effects on "crystallites" of reasonable size. Currently, primary recoil energies are limited by the crystallite size to 100–200 keV which is more than adequate to give significant insights into spike processes with simulations running up to times of tens of picoseconds after the simulated impact.

In 1981 in a review of high-density cascade effects, Thompson (1981) posed two interesting questions on the nature of spike processes and these remained substantially unresolved until the last decade. The questions were: (i) "is it legitimate to use the concept of a vibrational temperature when the number of atoms in the spike (typically of the order of 10^4) may not be sufficient to be described by Maxwell–Boltzmann statistics?" and (ii) "is the duration of the spike (typically of the order of 10^{-11} seconds) sufficient for any major mass transport to occur?"

Recent TEM and MD work has conclusively answered question (ii) with at least empirical implications for question (i). In this sense the question of plastic flow resulting from spike effects is a solved problem in ion beam science as the next few paragraphs will illustrate.

2.2. Crater Formation

Using a facility at Argonne National Laboratory in which an ion beam is incident on thin foil specimens *in-situ* in a TEM (Allen et al., 1989), Donnelly and Birtcher (1999) studied the effect of single-ion impacts on the surfaces of a number of metals. Typically, in these experiments the specimen was tilted 15° towards the ion beam so that both ions and electrons were incident on the specimen at 15° to the foil normal and specimens were irradiated with Xe^+ ions at energies in the range 50–400 keV at fluxes of order 10^{11} ions/cm^2/s. The Au films were of thickness approximately 60 nm, made by thermal evaporation onto heated NaCl.

By defocusing the objective lens of the microscope (in a similar way to that generally done when imaging bubbles and voids), surface features arising from single ion impacts were imaged. Images were obtained under bright-field conditions, on regions of the (somewhat bent films) in which no Bragg reflection was strongly excited. Under such conditions, approximately 1000 nm of defocus of the objective lens yields images in which depressions (e.g. craters) on either surface of the foil are seen as areas of lighter contrast than the background and may be delineated by a dark Fresnel fringe. Similarly a small mound or particle on the surface appears darker than the background and may have a light fringe around it. A similar degree of overfocus gives rise to images in which this contrast is reversed. i.e. small craters appear darker than the background and small particles appear lighter than the background. In these experiments, at the magnification generally used (100 000), the area under observation measured approximately 110×85 nm and images of this area were recorded on videotape with a time resolution of a single video frame (1/30th second) and, at the flux used in the experiments (2.5×10^{11} ions/cm^2/s), approximately 20 ions impact on this area every second. With creation rates of between 0.02 and 0.05 craters per ion on Au, this results on average in a new crater appearing in the 110×85 nm area every 1–2

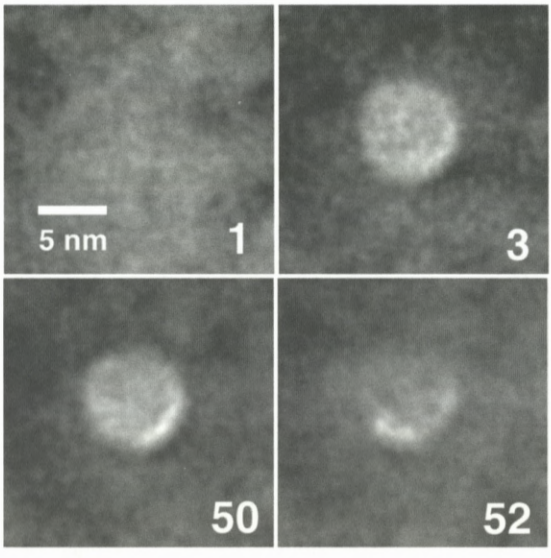

Figure 1. The creation and subsequent annihilation of a crater as a result of impacts of individual 400 keV Xe ions. Experiments carried out a room temperature. The numbers are video frame numbers (i.e. time steps in units of 1/30 s). Experiments carried out a room temperature. From Donnelly et al. (2005).

seconds. However, as will be discussed later, craters are unstable under irradiation and are rapidly filled in by material transported from other impact sites. This can be clearly seen in the "Craters" video-clip which can be streamed or downloaded via the internet (Donnelly, 2006).

The video-recording thus gives the impression of a surface exhibiting almost fluid-like properties on which a crater (sometimes along with expelled material) suddenly appears and then disappears over several seconds, during which time new craters appear. A frame-by-frame analysis, however, reveals that both crater creation and the flow that causes crater annihilation are discrete processes resulting from single ion impact effects. By using stereoscopic techniques it was also possible to show that for 400 keV irradiations, craters appeared on both the entrance and exit surfaces of the film – consistent with the results of simulations of energy/damage distributions in gold, using the Monte-Carlo code SRIM (Ziegler et al., 1985) which indicate that, in a 60 nm foil, energetic collisions take place near both surfaces at this energy.

Figure 1 shows a sequence of four images, digitized from videotape, of the same area of the gold foil. A crater is formed by a single ion impact, survives unchanged for just under two seconds and then is partially annihilated by a subse-

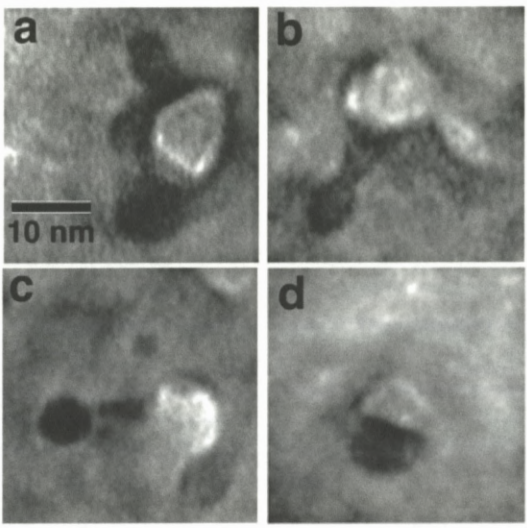

Figure 2. Examples of large features (consisting of craters and expelled material) on Au resulting from single ion impacts of Xe ions at energies of (a) 200 keV and (b) and (c) 400 keV. The images have been digitized from video recordings. Note that the imaging conditions ($\approx$1000 nm of objective lens underfocus) that give rise to craters appearing with a lighter contrast than the background, give rise to the observed darker contrast for expelled material on the surface of the foil. See text for details. Experiments carried out a room temperature. From Donnelly et al. (2005).

quent ion impact. The numbers on each part of the figure indicate the video-frame from which the image was taken and thus indicate the passage of time in units of 1/30th second. An important aspect of the study illustrated here is the general observation that craters are annihilated by subsequent individual ion impacts. As a result of this, experiments in which specimens were ion irradiated and then subsequently examined "post-mortem" for craters by TEM, such as the work by Merkle and Jäger (1981), significantly underestimated crater creation efficiencies. This is an example where *in-situ* TEM observations are essential if the dynamics of the process are to be understood.

Although the creation and annihilation of the regular crater shown in Figure 1 give little clue to the mechanisms responsible, these can be more easily gleaned from the images shown in Figure 2 where four craters resulting from impacts of Xe ions on Au at energies of (a) 50 keV, (b) 200 keV and (c) and (d) 400 keV Xe are shown. In each case, the crater appeared between successive video frames and thus resulted from a single ion impact. In particular, Figures 2b and 2c are strongly indicative of an expelled liquid droplet – fully separated from the crater in Figure 2c. This conclusion is confirmed by MD simulations of Xe ion irradiation

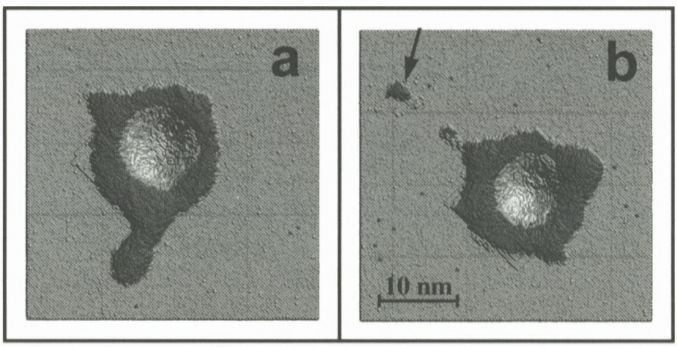

Figure 3. Structures observed in molecular dynamics simulations of impacts of 100 keV Xe ions on Au surfaces. In these images, the lighter shaded atoms are below the original surface and the darker shaded ones above. The arrow in panel "b" indicates a particle ejected from the crater by means of a "slingshot" process. From Donnelly et al. (2005).

of a {100} Au surface by Nordlund et al. recently reviewed by Donnelly et al. (2005) which exhibit a range of crater morphologies matching those observed experimentally. Examples of these are shown in Figure 3 in which MD simulations of single heavy-ion impacts have resulted in the formation of craters surrounded by expelled material and a small expelled droplet as indicated by the arrow in Figure 3b.

The comparison of the experimental results with those of the MD work makes it clear that, for many craters, there has been significant mass transport of material from the impact site, answering Thompson's question (ii) in the introduction in the affirmative. Also experimentally, the form of the expelled material (i.e. not having the same shape as its crater) provides qualitative evidence that it may have been expelled as a liquid droplet and this is exactly borne out by the MD work. Regardless of whether or not the spatial and temporal dimensions of the spike are sufficient to permit the use of Maxwell–Boltzmann statistics, the images and simulations indicate that macroscopic concepts such as melting and flow in response to surface tension forces, and quenching, provide a satisfactory description of the spike-induced crater creation process.

Although, in the majority of craters where expelled material could be seen, the above description seems appropriate, in a number of instances, small craters occasionally appeared to be accompanied by a solid plug of material having the approximate form of the crater. Such a crater is illustrated in Figure 2d). This is similar to the "lid" images recorded by Merkle and Jäger (1981). For such craters, we follow the interpretation of Merkle and Jäger that these result from spikes a sufficient distance below the surface such that a solid disc of material is

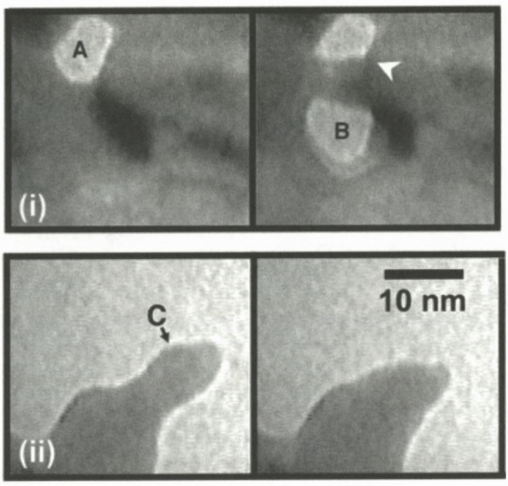

Figure 4. Microstructural evolution in Au during 200 keV Xe irradiation at room temperature: (i) the creation of a hole (B) by the impact of a single 200 keV Xe^+ ion, (ii) the change in shape of a protruding part of the gold foil following a single impact in the region indicated by "C". In each case the pair of images has been digitised from successive frames of a video-recording of the *in-situ* experiment. Experiments carried out a room temperature.

punched out by the large pressure increase that accompanies the thermal spike. MD simulations of 10 keV self ion impacts on gold (Averback and Ghaly, 1994) indeed indicate that large pressures as well as large temperatures may occur in a spike, albeit for very short periods.

2.3. Hole Formation

Finally, in an experiment in which a wedge-shaped, electro-chemically thinned gold foil was irradiated with 200 keV Xe ions, individual ion impacts were observed to produce holes through the thinnest areas of the foil (estimated to be 20–30 nm in thickness). Such an event can be seen in Figure 4(i) in which the two panels are separated by a single video frame. The light areas are holes punched entirely through the foil. Hole "B" forms due to a single ion impact next to pre-existing hole "A" which is partially filled in, in the area indicated by the arrow, by material expelled from hole "B". In addition, impacts at the edges of the foil could be seen to cause localised melting followed by a thickening of the material under the influence of surface tension forces as shown in Figure 4(ii) in which the two panels are again separated by a single video frame. This "pulsed, localized flow" resulted in a relatively rapid loss (by thickening rather than sputtering) of the thin areas of the foils. A much clearer picture of these process than it is possible

to convey from static images is to be seen in the video-clip "Holes" (Donnelly, 2006).

3. Inert Gas Bubbles in Solids

3.1. Background

Technological interest in inert gases in solids stems primarily from materials problems associated with the operation of both fission and fusion reactors. Inert gases, that are either directly injected or result from transmutation reactions in the reactor materials, tend to agglomerate at regions of low electron density and may form high concentrations of nanometre-sized bubbles. This can result in lifetime-limiting problems for reactor components such as grain-boundary embrittlement, swelling, blistering and exfoliation. More recently, however, cavities deliberately formed by ion implantation of helium into silicon have been investigated as possible proximity gettering sites for transition metal impurities. In all cases, a fundamental understanding of the nucleation and growth processes are of importance in dealing with the technological issues.

3.2. Growth Mechanism for Helium Bubbles in Silicon

Small helium bubbles are observed to form in silicon following ion implantation at room temperature. Subsequent annealing, at temperatures of 800°C or higher, results in the growth of the bubbles and the out-diffusion of the gas to yield the larger facetted voids which are of interest for potential use in the gettering of metallic impurities (Petersen et al. 1997). Until recently, an unsolved problem in ion-beam physics was the mechanism of bubble growth in helium-implanted silicon. Although a theoretical analysis by Evans (2002) had indicated that the operative mechanism should be motion and coalescence, rather than Ostwald ripening, experimental evidence on this issue was ambiguous.

This is a problem that is clearly, in principle, resolvable by TEM observations using a hot stage in which the growth of the cavities could be directly observed. Unfortunately, however, even at the moderate magnifications (≈50 000–100 000) necessary to image nanometer-sized cavities, thermal drift when using the hot-stage renders direct observation of cavity growth difficult. The area of interest drifts significantly as the temperature is raised and is periodically brought back into the centre of the field of view of the video camera resulting in a very "jerky" video sequence – particularly when the sequence is speeded up in an attempt to deduce the cavity growth mechanisms. By the time the drift has reduced to a degree that enables individual cavities to be observed, most of the motion and

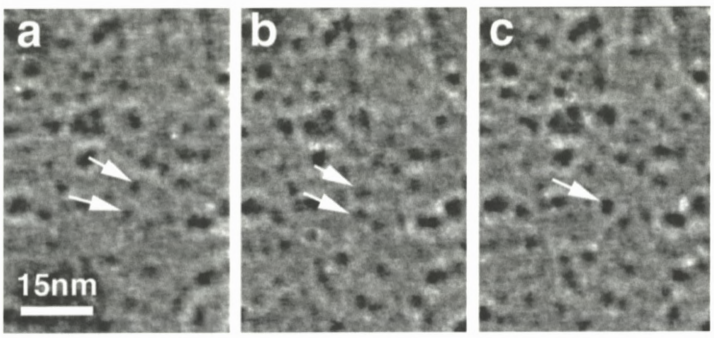

Figure 5. Bright-field underfocused images digitised from a video-recording of an annealing experiment on helium bubbles in silicon. (Note that the contrast has been reversed for clarity of reproduction.) The time interval between successive images is 3.3 seconds. The two cavities indicated by arrows in (a) have moved closer together in (b) and have coalesced into the single bubble indicated by the arrow in (c).

coalescence has occurred. Cavities are observed to have grown or disappeared due to coalescence but the motion that has led to this is not directly observed leading to the false conclusions that growth has occurred by Ostwald ripening (Donnelly et al., 2001). This is illustrated in two video clips (Donnelly, 2006). "HeBub01" is a real-time sequence which illustrates the degree of drift during an annealing experiment. "HeBub02" is a sequence that has been speeded up by a factor of 25 in which considerable bubble growth takes place; however, it is extremely difficult either by viewing the video-clip or by examining consecutive single frames to determine the mechanism of bubble growth.

The effects of this thermal drift can, however, be largely removed by centering and cropping the individual frames that make up the video-clip and reassembling the treated frames into a new video sequence. "HeBub03" (Donnelly, 2006) is a short clip, speeded up by a factor of 100, that has been treated in this way. It is perfectly clear from this clip that considerable bubble movement is taking place and that, in this temperature interval (780–840°C), cavity growth unequivocally takes place by motion and coalescence. Figure 5 shows three frames taken from this clip and illustrates the difficulty of making deductions from the static images. Having viewed the video-clip, it is fairly clear that, for instance, the bubbles indicated by the arrows undergo relative motion and coalescence. However, it would be difficult by analysis of the static images alone, to come to unambiguous conclusions regarding growth mechanisms.

During random (Brownian) motion in a solid, when a cavity migrates in any particular direction, there must be transport of substrate atoms in the opposite

direction or (equivalently) motion of vacancies in the same direction. This can occur either as a result of the diffusion of vacancies and/or interstitials through the bulk solid or by the motion of adatoms and/or surface vacancies at the surface of the cavity. Bulk diffusion in silicon occurs at an energy of 4.75 eV (Bracht et al., 1998) and thus will not be relevant at the temperatures of interest here ($\leq$1000°C). Surface diffusion occurs with a lower activation energy and is likely to be the relevant mechanism of cavity motion in the temperature range of interest.

Diffusivity is proportional to the square of the step length and the jump frequency, ν. Allen et al. (1999) have shown that, for a cavity, the step length is given by λ/N, where λ is the atomic jump distance and N is the number of vacancies in the cavity and that the cavity diffusivity, D_c, can thus be written as:

$$D_c = \frac{1}{4}\left(\frac{2\lambda}{N}\right)^2 \nu, \tag{1}$$

where the factor of 1/4 arises for observed projected displacements. Using the proportionality between r.m.s. displacement and $\sqrt{D_c t}$, where t is time, Birtcher et al. (1999) have derived the following equation for the r.m.s. distance, r_{rms}, moved by a cavity in time interval Δt:

$$r_{rms} = 2\frac{\lambda}{N}\sqrt{\nu_0 \, e^{E_s/kT} \Delta t}, \tag{2}$$

where E_s is the activation energy for surface diffusion, ν_0 is the jump attempt rate, T is temperature and k is Boltzmann's constant. This leads to the following expression for the cavity velocity, v_c, along the projected path, observed from successive video frames recorded with a frame rate of $1/\Delta t$:

$$v_c = 2\frac{\lambda}{N}\sqrt{\frac{\nu_0 \, e^{E_s/kT}}{\Delta t}}, \tag{3}$$

where Δt is 1/30 second.

Surface diffusion on silicon surfaces has been measured using scanning probe microscopy techniques to have activation energies varying from 1.3 eV to 2.1 eV for different surfaces ({100} and {111}) under different experimental conditions (Kitamura et al., 1993; Ichimiya et al., 1997). Using Equation (3) and taking an intermediate value of E_s of 1.7 eV, which has been identified as the diffusion energy of dimer vacancies on a {100} Si surface (Kitamura et al., 1993), v_c has been plotted as a function of bubble radius for a number of different temperatures in Figure 6. From this figure it can be seen that at 800°C, a cavity of radius between 20 and 40 Å would migrate at a speed from 10 to 1 Å/s – approximately consistent with the motion observed in the processed video-clip "HeBub03".

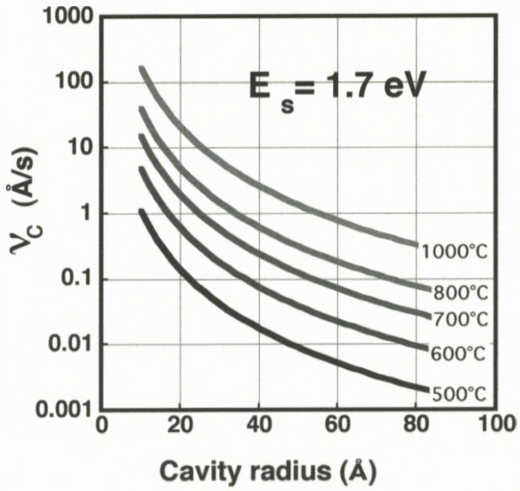

Figure 6. Calculated rate of movement of cavities at different temperatures due to surface diffusion with an activation energy of 1.7 eV as a function of radius. See text for details. From Donnelly et al. (2001).

Cavity growth in silicon thus has been unequivocally shown to occur by surface-diffusion induced motion and coalescence, in agreement with the theoretical findings of Evans (2002) and is thus now a solved problem in ion-beam physics.

3.3. Solid Xe Bubbles in Al – Background

Inert gas atoms generally have negligible solubility in metals and, as in the case of silicon, condense into nanometer-sized gas-filled cavities. Although research on inert gases in solids in general and in metals in particular has been undertaken for many decades and has established many aspects of their behaviour, until recently there have been a number of unanswered questions regarding their behaviour. For the heavier gases, in some circumstances, the inert gas in the cavities may be in solid form at room temperature so that "precipitate" probably provides a more useful description than "cavity" or "bubble". The high (Gigapascal) pressures necessary for the gases to be solid at room temperature result from simple surface energy or surface tension considerations: gas within a small three-dimensional vacancy cluster will prevent its collapse to a vacancy-type dislocation loop. For

a spherical cavity of radius R, an equilibrium pressure of P_{EQ} will prevent this collapse and result in a cavity with no stress in the surrounding material where:

$$P_{EQ} = \frac{2\gamma}{R}, \tag{4}$$

where γ is the interface free energy, which in the case of an inert gas precipitate will be close to the value for the free surface. In principle, the pressure given by Equation (4) may be a lower bound to the pressure within such precipitates with the upper limit being determined by the pressure necessary to punch a dislocation loop, P_{LP}, which has been shown by Trinkaus (1983), following Greenwood et al. (1959), to be approximately given by:

$$P_{LP} = \frac{2\gamma}{R} + \frac{\mu b}{R}, \tag{5}$$

where μ is the shear modulus of the substrate and b is the magnitude of the burgers vector of the dislocation loop (assumed to have the same radius as the precipitate). For a cavity of radius 1 nm in aluminium, Equations (4) and (5) yield pressures of approximately 2 and 9 GPa respectively.

In the 1980s, researchers first identified solid precipitates of argon, krypton and xenon in a variety of fcc metals in electron diffraction experiments and found that the precipitates were epitaxial (but non-commensurate) with the substrate (Templier et al., 1986). In hcp metals the precipitates were observed themselves to have an hcp structure again epitaxial with the substrate (Evans and Mazey, 1986), and in bcc metals they were observed to have an fcc structure with the densely packed (111) planes in the inert gas in contact with the densely packed (110) planes in the metal (Templier, 1991). The pressures determined from lattice parameter measurements obtained from diffraction patterns, coupled with bulk equations of state indicated that the precipitates were, in general, close to the equilibrium pressure given by Equation (4). The inevitable creation of vacancies (and interstitials) during the injection of inert gases by ion implantation presumably ensures that sufficient vacancies are always available for pressure equilibration to take place.

The detailed structure of inert gas precipitates was subsequently elucidated by high-resolution phase contrast electron microscopy (Donnelly and Rossouw, 1985; Birtcher et al., 1999) and a typical high resolution image of a Xe precipitate in Al is shown in Figure 7 (details of how this image was obtained will be presented below). The precipitates are generally observed to be of a tetradecahedral shape – that is an octahedral cavity bounded by {111} planes, truncated by 6 {100} facets. This shape and its projection along two low index directions is also illustrated in Figure 7.

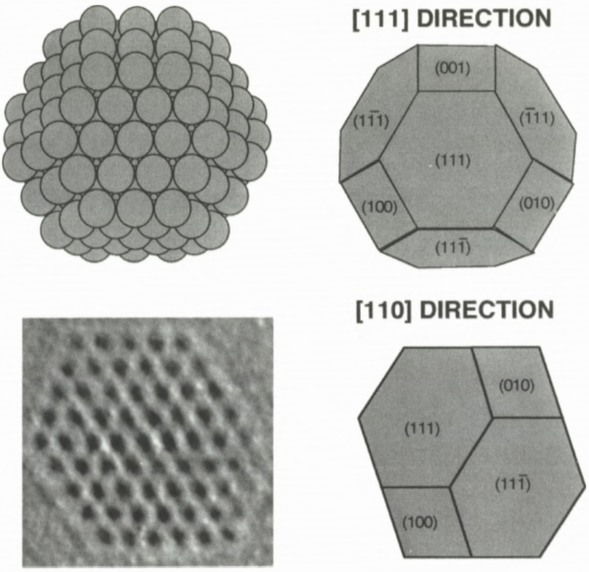

Figure 7. Schematic illustration of the tetradecahedral form of Xe precipitates in Al. Right-hand images are two different projections of the precipitate. The lower, left hand image is a high-resolution electron micrograph of a Xe precipitate in Al where the black contrast is from the Xe atom columns viewed along [110]. See text for details.

As in the case of He bubbles in Si, Xe precipitates in Al also grow on annealing and if this is as a result of motion and coalescence it is unclear as to how that process might occur – particularly given the fact that the inert gas within the cavity is in solid form. Questions that required answering in this regard include:

(i) Do solid inert gas precipitates grow by motion and coalescence?
(ii) If so, by what mechanism does a solid precipitate migrate?

and, as precipitates are generally observed to be close in shape to that shown in Figure 7:

(iii) What processes occur to bring a larger precipitate, formed by coalescence of two smaller ones, back to a compact, truncated octahedral shape?

3.4. High-Resolution Observations

These particular issues have been resolved by high-resolution TEM (HRTEM) work carried out using the JEM ARM-1000 high-voltage TEM at the National Institute for Materials Science in Tsukuba, Japan (formerly, the National Research Institute for Metals) and it is this that will be discussed below. The microscope was operated at a voltage of 1 MV and in general the HRTEM images were recorded with the incident electron beam tilted approximately 3° from an Al ⟨110⟩ direction in order to provide clear Xe images. A (non-Scherzer) defocus of approximately −76 nm was used essentially to filter out information from the aluminium substrate and provide clear Xe images (Furuya et al., 1998). Using a video camera and an on-line image processing system (giving a 5-frame average) images were obtained with sufficient contrast and intensity to be recorded directly onto standard S-VHS videotape at a frame rate of 30 s^{-1}. With the frame averaging, the temporal resolution of the system was thus 1/6 second. The specimens were 3mm Al discs (99.999%-pure) thinned by electropolishing. Ion implantations were carried out at room temperature with 30 keV Xe ions to a fluence of 2×10^{16} ions cm^{-2}. Some specimens were then vacuum-annealed at 300°C for 30 minutes to reduce radiation damage within the substrate and to consolidate the Xe within the precipitates.

3.4.1. *Precipitate Shape Change*

High voltage microscopy is *not* a non-perturbatory experimental technique. A 1 MeV electron may transfer up to 161 eV to an aluminium and also 33 eV to a Xe atom. This will result in displacements in the Al and probably in the Xe also (the displacement energy is not known in solid Xe). In addition a 161 eV Al recoil can transfer a maximum of 91 eV to a Xe atom. Under the viewing conditions used for the experiments a displacement rate of approximately 1 dpa per minute for the aluminium has been estimated. This high displacement rate means that the precipitates are continually interacting with a significant flux of vacancies and interstitials the effects of which can be seen in the video-clip "XeAl01" (Donnelly, 2006) and in still frames captured from the clip and shown in Figure 8.

The figure shows four images of a single Xe precipitate taken at different times (indicated in seconds in each image) from an arbitrary starting time. The images were recorded with the electron beam incident close to a ⟨110⟩ zone axis, under conditions such that contrast from the Al is faint but the Xe atom columns are clearly visible as black spots. The precipitate at $t = 0$ is clearly faceted and the image is consistent with a [110] projection of a truncated octahedron as shown in Figure 7 although it has departed somewhat from the equilibrium Wulff net shape (Wulff, 1901).

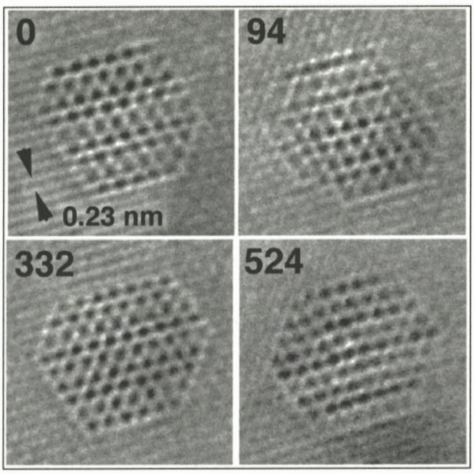

Figure 8. HRTEM images digitised from videotape of a Xe precipitate in Al undergoing shape changes induced by 1 MeV electron irradiation. Each image is an average of 5 frames. Numbers indicate time in seconds. From Donnelly et al. (1997).

With the exception of the image taken at 94 seconds, the images in Figure 8 all appear to correspond to a projection of this 14-sided shape but with facets of varying size. At 94 seconds, the precipitate departs somewhat from this shape as a consequence of having "missing" atoms at one vertex of the structure.

In many images (e.g. $t = 0$ image in Figure 8), {111} Al fringes are visible enabling a comparison to be made between the Xe and Al interplanar spacings. The ratio of the lattice constants of the two materials exhibits values ranging from about 1.4–1.5 yielding a lattice constant for the Xe in the range 0.57–0.61 nm. Assuming that a macroscopic equation of state (EOS) is valid for such small particles and using an EOS due to Ronchi (1980) the atomic density that this range of lattice spacing represents, corresponds to pressures between approximately 10 and 30 kbar.

The projected "radius" of the precipitate in Figure 8 is in the range 1.2 to 1.5 nm for which Equation (2) yields values in the range 15–18 kbar; implying that the precipitate is probably close to equilibrium pressure.

The impact of 1 MeV electrons with aluminium atoms in an Al plane immediately in front of the Xe precipitate (w.r.t. the electron beam) will tend to inject Al atoms into the Xe. Such atoms may be expected to diffuse through the Xe to one of the 14 planes making up the Al cavity. This clearly will have a randomising effect on the cavity shape; however the Al adatoms arriving on the cavity facets might be expected to surface diffuse until becoming trapped at a

ledge or vertex. In time, this process may result in the growth of an extra plane of atoms on a facet. Essentially, this is a process whereby Al atoms are transferred from one facet to another. In addition, electron impacts with the Al atoms in the rear facets of the cavity (w.r.t. electron beam) will leave additional Al vacancies at the surface of the cavity thus randomising the atomic arrangement on the facet and augmenting the cavity volume. However, the precipitate will also interact with the large numbers of mobile vacancies and self-interstitial atoms (SIAs) caused by displacement events in the aluminium. In this way, the system will act to keep the precipitate at equilibrium pressure (thus preventing any net growth) with a shape tending towards the minimum energy form defined by the Wulff construction (Wulff, 1901).

The predominant impression that is gained from viewing the speeded-up video-clip "XeAl01" is that the cavity containing the Xe is continually and randomly changing its shape by the growth or removal of planes of atoms on facets and that the Xe, always retaining its crystalline structure, is "repacking" itself into the altered cavity shape. Room temperature Xe at high pressure is a solid with a very low shear modulus so that, in the video clip, the Xe is seen to adapt to the changing shape of the cavity by shear processes. The overall effect is to cause a random variation of the position of the centre of mass of the precipitate causing it to undergo a degree of stochastic (Brownian) motion, similar to that caused by surface diffusion processes in the helium-induced cavities in Si.

3.4.2. *Precipitate Motion*

The effect of this process on a small cluster can be seen in video clip "XeAl03" (Donnelly, 2006) where such a cluster can be clearly see to migrate. Two frames from this video sequence are shown in Figures 9a and 9b. The frames are separated by 23 seconds and the cluster has moved approximately 1 nm in this time. Figure 9c shows an image of this small cluster in which it has a symmetric form from which (on the assumption of square {100} facets) one can deduce that the cluster contains 38 Xe atoms as shown in Figure 9d.

3.4.3. *Coalescence*

As in the case of thermally-induced motion, this displacement-induced motion will result in the coalescence of the Xe precipitates and, indeed the precipitate distribution is seen to coarsen under continued electron irradiation. The coalescence of two solid precipitates can be seen in the video-clip "XeAl05" (Donnelly, 2006) and four frames from this clip are shown in Figure 10. The stochastic motion discussed above is observed to result in the two precipitates coming within approximately 0.5 nm of one another, at which time the two atomic planes of Al separating them ruptures leading to coalescence into an initially elongated precip-

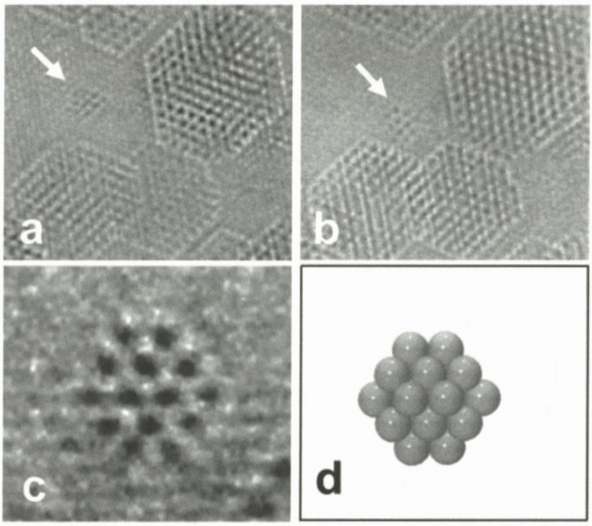

Figure 9. Motion of Xe cluster during continuous 1 MeV electron irradiation. (a) Small Xe cluster indicated by arrow. (b) Small Xe cluster 23 seconds later. Cluster has moved approximately 1 nm between images. (c) Higher magnification image of cluster in symmetrical configuration. (d) Model of small cluster containing 38 atoms.

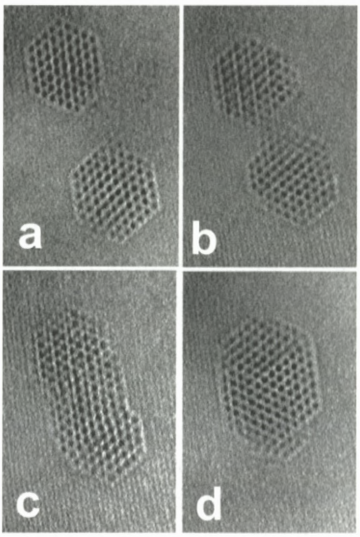

Figure 10. Coalescence of two Xe precipitates in Al during continuous 1 MeV electron irradiation. Time intervals between images are: (a)–(b) 132 seconds; (b)–(c) 34 seconds; (c)–(d) 143 seconds. From Birtcher et al. (1999).

itate. Under the continuous defect flux, however, the precipitate rapidly evolves towards the minimum-energy Wulff net shape and during these changes the Xe remains solid but repacks itself into the cavity by a multiple shearing process as described previously. Note that the large precipitate formed by the coalescence of the two smaller ones is still small enough to have an equilibrium pressure sufficiently high to keep the xenon in the solid state.

This work has clearly provided answers to the questions posed at the start of this section regarding the mobility of solid embedded nanoprecipitates. Specifically, (i) solid inert gas precipitates grow by motion and coalescence under a flux of vacancies and interstitials resulting from displacing electron irradiation. It is highly likely that the same growth process will also obtain during thermal annealing. (ii) The migration mechanism, under displacing irradiation is an interaction with the defect flux that yields changes in the shape of the cavity (without any net volume change) giving rise to a stochastic movement of the centre of mass of the precipitate. In the case of thermal annealing it is likely that similar motion will result from surface diffusion processes as with He in Si. Finally, (iii) the interaction of the cavity with defect fluxes as analysed by Allen et al. (1999) results in a precipitate, formed by coalescence of two smaller ones, evolving rapidly towards the low energy Wulff net shape. For a rigid material within the cavity this could not occur; however, having very low shear modulus, the room-temperature solid inert gas simply repacks itself into the modified shape by shear processes.

All of these are thus solved problems; however, the video clip "XeAl04" (Donnelly, 2006) illustrates one aspect of the behaviour of solid Xe precipitates in Al which remains unexplained.

3.4.4. *Reversible Melting*

The clip illustrates one cycle of a melting/solidification process that occurs up to 4 or 5 times for some precipitates. Frames from this clip are shown in Figure 11. It should be noted that the observed change in contrast does not unequivocally imply that the precipitate has melted – it could simply have rotated within the cavity. However, a detailed investigation at a range of tilts, as well as the observed volume change of the precipitate (see below) indicates strongly that the precipitate does indeed melt. This reversible melting and solidification is difficult to understand, given that the defect flux remains constant during this process. Note that the process appears to be firstly melting followed by a much slower volume change by up to 30%. The volume change then reverses and the precipitate returns slowly to its original volume whereupon it is observed to recrystallise.

A possible explanation could perhaps lie in the creation of sufficient radiation damage within the precipitate such that the Xe is ballistically amorphised, giving

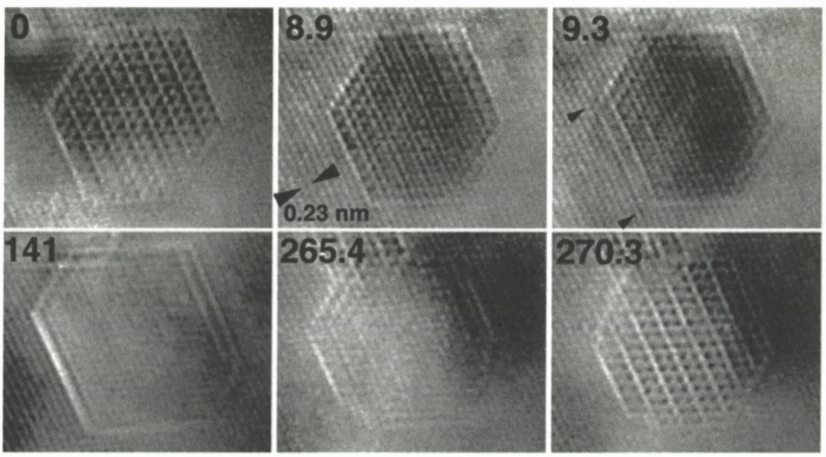

Figure 11. Melting and resolidification of Xe precipitate during continuous 1 MeV electron irradiation. Time, in seconds, is indicated on each panel.

rise to a sudden pressure increase that would (via strain fields around the precipitate) result in a greater uptake of vacancies to equilibrate the surface tension and pressure via Equation (4) thus increasing the volume. Reordering processes within the Xe may subsequently enable the precipitate to recrystallise and, by packing more efficiently, reduce its pressure so that, again by interaction with the defect fluxes, the volume would reduce. This hypothesis is currently being modelled by molecular dynamics to test its feasibility.

The reversible melting and solidification of Xe precipitates in Al under displacing electron irradiation thus remains an unsolved problem.

4. Amorphous Zones in Silicon

4.1. Background

Amorphous layers of silicon on crystalline silicon have been studied fairly extensively for over 20 years, and it has been well established that they can be re-grown to crystallinity by motion of the planar interface into the amorphous layer by thermal annealing at temperatures of 550°C or above (Jackson, 1986). Many mechanisms have been invoked to explain this re-crystallization process. These generally involve the movement and/or generation of defects at the amorphous-crystalline interface with possible defects including dangling bonds (Jackson, 1986), charged kinks on terraces (Williams and Elliman, 1983) and the so-called "bond defect" or I-V pair (Weber et al., 2000; Pelaz et al., 2004). The recrystalliza-

tion process, for the planar interface is characterized by a well-defined activation energy of 2.7 eV (Jackson, 1986).

For partially amorphized Si, where pockets of amorphous material are surrounded by crystal, the situation is more complex. Recrystallization may take place thermally and as a result of electron irradiation. For thermally induced recrystallization, amorphous zones have been observed by TEM and by Rutherford Backscattering Spectroscopy to recrystallize at lower temperatures than the continuous amorphous layer and over a wider range of temperatures.

4.2. In-Situ Observations

By ion irradiating *in-situ* in the TEM – with the specimen in a heating stage permitting subsequent annealing experiments – it is possible to follow the entire life-cycle of individual amorphous zones rather than simply obtaining averaged statistical data. Such experiments were carried out using the *in-situ* TEM/ion accelerator facility referred to in an earlier section (Allen et al., 1989) in which the ion beam is oriented 30° from the microscope axis. For this work, however, the electron energy was kept to 100 keV in order to minimize electron-beam annealing of the amorphous zones (Jencic and Robertson, 1996). Amorphous zones were imaged using structure-factor contrast (Ashby and Brown, 1963) under down-zone, bright-field conditions with the electron beam normal to the {110} surface. The recrystallization behavior of a large number of individual zones was followed on a series of negatives following different isochronal annealing steps. Recrystallization of a smaller number of zones was followed in real time during a slow temperature increase by recording on videotape.

Amorphous zones (a-zones) ranging in size from approximately 1 to 10 nm in size are observed to recrystallize over a range of temperatures from about 70°C to 400°C (Donnelly et al., 2001). In addition, however, the *in-situ* measurements yield the observation that zones with closely similar initial sizes may recrystallize at significantly different temperatures. This is illustrated in Figure 12 where three a-zones, all just over 2 nm in radius, were observed to recrystallize at temperatures of approximately 100°C, 200°C and 300°C respectively. A further indication of the diversity of behaviour observed in these experiments is presented in Figure 13 in which an area of a specimen irradiated to a fluence of 1.25×10^{12} ions cm^{-2} with 200 keV Xe ions at room temperature is shown. The top panel shows a number of a-zones following the irradiation. The bottom panel shows the same area after a 10 minute isochronal anneal at 115°C (with two prior 10 minute anneals at 75°C and 95°C; images following which are not shown).

The large zones, marked "A" and "B" and "C" on the figure not only shrink significantly, but also to tend towards a more spherical shape (a more circular

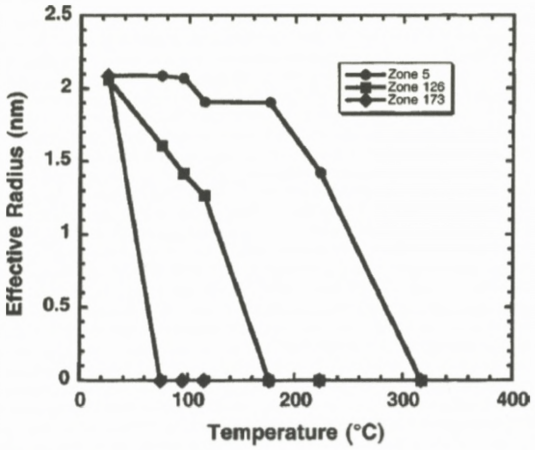

Figure 12. Change in effective radius of three individual amorphous zones with same starting radius following 10 minute anneals to successively higher temperatures. From Donnelly et al. (2003).

shape in projection), i.e. the regions of the a/c interface with small convex radii of curvature appear to recrystallize first. The smaller zones, indicated with an "x" in the figure appear to have completely recrystallized. Larger zones have thus shrunk and smaller zones have disappeared; however, a zone of intermediate size, "E" remains virtually unchanged. This diversity in behaviour is typical of the 500 zones whose individual lifecycles have been studied. The size of an a-zone does not uniquely determine the temperature at which it will recrystallize, and it is not possible to define a unique activation energy for the recrystallization process. Finally, the zone marked "D" in the bottom panel of Figure 13, despite being initially smaller than the zones marked "x" that have disappeared by 115°C, can be seen to grow following the annealing step. This type of "reverse annealing" process is seen in approximately 2% of the zones.

Questions to be resolved regarding the recrystallisation of amorphous zones thus include:

(i) Why is recrystallization, even for zones of similar starting size not characterized by a well-defined activation energy?
(ii) Why does recrystallization proceed in a small number of steps consisting of rapid reductions in size interspersed by longer plateau during which the size stays constant?
(iii) Why, in a small number of cases, do zones grow during an annealing step?

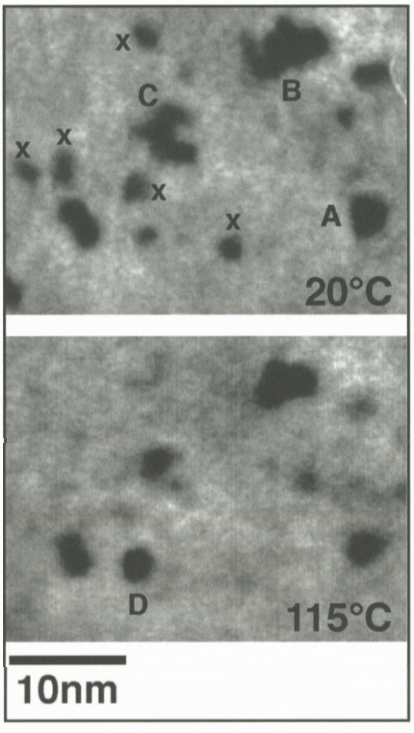

Figure 13. Amorphous zones produced by single impacts of 200 keV Xe ions in Si following creation at 20°C (top panel) and three 10 minute isochronal anneals at 75°C, 95°C and 110°C (bottom panel). See text for details.

In recent work involving both molecular dynamics (MD) and Monte-Carlo modelling of the amorphization and recrystallization of silicon, Pelaz et al. (2004) have investigated the atomistics of irradiation-induced amorphization of silicon. In this work they have focused on the so-called "bond defect" or I-V pair and its role in amorphization and recrystallization. This defect consists of a coupled interstitial and vacancy and contains 5 and 7 member rings characteristic of amorphous silicon. A volume of Si containing approximately 25% of I-V pairs has a radial pair distribution function essentially indistinguishable from amorphous silicon quenched from the melt. An isolated I-V pair has a recombination energy of only 0.43 eV and is thus not stable at room temperature. However, this recombination energy increases as the number of neighboring I-V pairs increases. For an I-V pair at the interface of an amorphous zone with crystal, this activation energy will depend on the local radius of curvature. This gives rise to variable recrystallization kinetics as seen in our experiments – with zone size, zone shape and interface

roughness all playing roles in determining the effective activation energy. For instance, the steplike behaviour seen experimentally in the recrystallization of individual zones is easily explained by this model: for a spherical zone, I-V pairs lying on the a/c interface will have the same co-ordination (i.e. the same number of neighbouring I-V pairs). The zone will remain stable until one of these IV pairs recombines, leaving a crystalline "hole" at the a/c interface. The I-V pairs around this hole now each have one fewer neighbour and therefore will recombine faster. The initial I-V pair recombination thus acts as a trigger for the recombination of the surrounding I-V pairs (Pelaz et al., 2004).

In addition, Lopez et al. (2004) have recently reported a kinetic Monte-Carlo simulation of an anneal at 400°C of two zones each containing approximately 500 atoms but with different shapes (approximately cubic and spherical respectively). The simulation exhibited significantly different average recrystallization rates (approximately a factor of two) and also exhibited plateaux and rapid steps exactly as observed experimentally.

The reverse annealing effect in which an amorphous zone *grows* rather than shrinks, following an increase in temperature, has not yet specifically been modelled. However, we speculate that, given the Gaussian nature of the energy deposition density radially outwards from the centre of the energy spike resulting from a single heavy ion impact, the zone morphology may consist of an amorphous core surrounded by a crystalline region in which a high density of point defects has been quenched in during the rapid decay of the thermal spike. This type of configuration has been seen in MD simulations (Caturla et al., 1996). Energetically, it may be favourable for this entire volume to become amorphous, rendering the growth of the zone possible when the temperature is raised.

Although, Pelaz's I-V pair model of silicon amorphization is not universally accepted, it does provide a consistent explanation of almost all aspects of the complex recrystallization behaviour of nanometre-sized amorphous zones. As such, it could be argued that the formation of amorphous zones by single-ion impacts in silicon and their thermal recrystallization is at least a tentatively solved problem. The remaining unsolved problem is the surprising observed growth of some amorphous zones on annealing. It is to be hoped that additional simulation work may serve to explain this phenomenon also in the light of the I-V model of silicon amorphization.

5. Conclusions

In summary, the *in-situ* TEM work carried out over the last decade or so on radiation damage processes in solids has had a good track record in providing

solutions to problems in ion beam physics; however, one or two puzzles remain. Specifically, the *in-situ* work has facilitated a fairly complete understanding of effects resulting from single heavy ion impacts on metal surfaces and, in particular, the importance of localised melting and flow processes have been highlighted.

For the work on single ion impacts on silicon, although arguments have been presented here that an explanation of Si amorphization in terms of I-V pairs would appear to be consistent with most experimental observations, this model is not accepted, at this juncture, by all researchers with an interest in the topic. And even in the context of the I-V pair model, the phenomenon of amorphous zone growth on annealing ("reverse annealing") is not fully understood.

Finally, although most of the behaviour of nanoscale Xe precipitates in Al under displacing electron irradiation can be understood in terms of stochastic changes to the Al cavity brought about by interactions with fluxes of vacancies and interstitials, the observed reversible melting of solid Xe precipitates remains an unsolved mystery.

Acknowledgements

I should like to acknowledge the major contribution of many colleagues in the work reported in this paper: in particular, Bob Birtcher and Charlie Allen of Argonne National Laboratory (both of whom have recently retired); Kazuo Furuya, Kazutaka Mitsuishi and Minghui Song of the National Institute for Materials Science; Vladimir Vishnyakov of Manchester Metropolitan University and finally, from my own institution, my career-long colleague and mentor, George Carter.

References

Allen C.W., Funk L.L., Ryan E.A. and Ockers S.T. (1989): In situ ion irradiation/implantation studies in the HVEM-tandem facility at Argonne National Laboratory. Nucl Inst Meth B **40–41**, 553–556

Allen C.W., Birtcher R.C., Donnelly S.E., Furuya K., Ishikawa N. and Song M. (1999): Migration and coalescence of Xe nanoprecipitates in Al induced by electron irradiation. Appl Phys Lett **74**, 2611–2613

Ashby M.F. and Brown L.M. (1963): On diffraction contrast from inclusions. Phil Mag **8**, 1649–1676

Averback R.S. and Ghaly M. (1994): A model for surface damage in ion-irradiated solids. J Appl Phys **76**, 3908–3910

Birtcher R.C., Donnelly S.E., Song M., Furuya K., Mitsuishi K. and Allen C.W. (1999): Behavior of crystalline Xe nanoprecipitates during coalescence. Phys Rev Lett **83**, 1617–1620

Bracht H., Haller E.E. and Clark-Phelps R. (1998): Silicon self-diffusion in isotope heterostructures. Phys Rev Lett **81**, 393–396

Brinkman J.A. (1954): On the nature of radiation damage in metals. J Appl Phys **25**, 961–970

Caturla M.J., Diaz de la Rubia T., Marque L.A. and Gilmer G.H. (1996): Ion-beam processing of silicon at keV energies: A molecular-dynamics study. Phys Rev B **54**, 16683–16695

Donnelly S.E. (2006): Video-clips available at: `http://www.imr.salford.ac.uk/fm/sed/media.php`

Donnelly S.E. and Birtcher R.C. (1999): Ion-induced spike effects on metal surfaces. Phil Mag **79**, 133–145

Donnelly S.E. and Rossouw C.J. (1985): High resolution electron microscopy of solid xenon bubbles in ion implanted aluminium. Science **230**, 1272–1273

Donnelly S.E., Furuya K., Song M., Birtcher R.C. and Allen C.W. (1998): 1 MeV electron irradiation of solid Xe nanoclusters in Al – An in-situ HRTEM study. In: Kirkland A. and Brown P.D. (Eds), Proceedings of the International Centennial Conference on the Electron. IOM Communications, Book 687, pp 306–312

Donnelly S.E., Vishnyakov V.M., Birtcher R.C. and Carter G. (2001): The effects of radiation damage and impurities on void dynamics in silicon. Nucl Instrum & Meth in Phys Res B **175–177**, 132–139

Donnelly S.E., Birtcher R.C., Vishnyakov V.M. and Carter G. (2003): Annealing of isolated amorphous zones in silicon. Appl Phys Lett **82**, 1860–1862

Donnelly S.E., Birtcher R.C. and Nordlund K. (2005): Single ion induced spike effects on thin metal films: Observation and simulation. In: Knystautas E.J. (Ed.), Engineering Thin Films and Nanostructures with Ion Beams. Marcel Dekker, New York, pp 7–78

Evans, J.H. (2002): Mechanisms of void coarsening in helium implanted silicon. Nucl Instrum & Meth in Phys Res B **196**, 125–134

Evans J.H. and Mazey D.J. (1986): Solid bubble formation in titanium injected with krypton ions. J Nucl Mat **138**, 176–184

Furuya K., Song M., Birtcher R.C., Allen C.W. and Donnelly S.E. (1998): Direct imaging of the atomic structure of Xe nanocrystals embedded in aluminium. In: Kirkland A. and Brown P.D. (Eds), Proceedings of the International Centennial Conference on the Electron. IOM Communications, Book 687, pp 341–347

Greenwood G.W., Foreman A.J.E. and Rimmer D.E. (1959): The role of vacancies and dislocations in the nucleation and growth of gas and bubbles in irradiated fissile material. J Nucl Mat **4**, 305–324

Ichimiya A., Tanaka Y., et al. (1997): Thermal relaxation of silicon islands and craters on silicon surfaces. Surf Sci **386**, 182–194

Jackson K.A. (1986): A defect model for ion-induced crystallization and amorphization. J Mater Res **3**, 1218–1226

Jencic I. and Robertson I.M. (1996): Low-energy electron beam induced regrowth of isolated amorphous zones in Si and Ge. J Mater Res **11**, 2152–2157

Kitamura N., Lagally M.G. and Webb M.B. (1993): Real-time observations of vacancy diffusion on Si(001)-(2x1) by scanning tunnelling microscopy. Phys Rev Lett **71**, 2082–2085

Lopez P., Pelaz L., Marquéz L.A., Santos I., Aboy M. and Barbolla J. (2004): Atomistic modeling of defect evolution in Si for amorphizing and subamorphizing implants. Mat Sci & Eng B **114–115**, 82–87

Merkle K.L. and Jäger W. (1981): Direct observation of spike effects in heavy-ion sputtering. Phil Mag A **44** 741–762

Pelaz L., Marqués L.A. and Barbolla J. (2004): Ion-beam-induced amorphization and recrystallization in silicon. J Appl Phys **96**, 5947–5976

Petersen G.A., Myers S.M. and Follstaedt D.M. (1997): Gettering of transition metals by cavities in silicon formed by helium ion implantation. Nucl Instrum & Meth in Phys Res B **127–128**, 301–306

Ronchi, C. (1980): Extrapolated equation of state for rare gases at high temperatures and densities. J Nucl Mat **96**, 314–328

Templier C. (1991): Inert gas bubbles in metals: A review. In: Donnelly S.E. and Evans J.H. (Eds), Fundamental Aspects of Inert Gases in Solids, Plenum, New York, pp 117–132

Templier C. et al. (1986): Transmission electron miscroscope study of xenon implanted into metals. Philos Mag A **53**, 667–675

Thompson D.A. (1981): High density cascade effects. Rad Eff **56**, 105–150

Trinkaus H. (1983): Conditions for dislocation-loop punching by helium bubbles. Rad Eff **78**, 189–212

Weber, B., Stock D.M. and Gärtner K. (2000): Defect-related growth processes at an amorphous/crystalline interface: A molecular dynamics study. Mat Sci & Eng B **71**, 213–218

Williams J.S. and Elliman R.G. (1983): Role of electronic processes in recrystallisation of amorphous semiconductors. Phys Rev Lett **51**, 1069–1072

Wulff G. (1901): Frage der Geschwindigkeit des Wachstums und der Anflösung der Krystallflachen. Z Krystall Min **34**, 449–530

Ziegler J.F., Biersack J.P. and Littmark U. (1985): The Stopping and Ranges of Ions in Solids. Pergamon Press, New York (see `http://www.srim.org`)